Nanoscale

Accepted Manuscript

This article can be cited before page numbers have been issued, to do this please use: C. Yang, V. Suresh, A. S. Rotelli, H. R. Sun, H. Liang, V. X. Ho, E. J. Teo and A. A. Bettiol, *Nanoscale*, 2025, DOI: 10.1039/D5NR02012C.

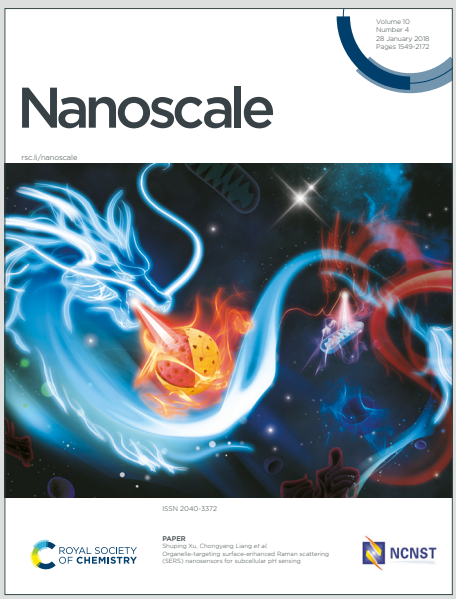

ROYAL SOCIETY OF CHEMISTRY

rsc.li/nanoscale

View Article Online
DOI: 10.1039/D5NR02012C

ARTICLE

Uniform Coating of Separated Nanodiamonds via Thin Polymer-assisted Electrostatic Self-Assembly for Thermal Sensing

Received 00th January 20xx,
Accepted 00th January 20xx

DOI: 10.1039/x0xx00000x

Chengyuan Yang, [a] Vignesh Suresh,[b] Aliki S. Rotelli, [a] Hui Rong Sun, [a] Haidong Liang, [a] Vinh Xuan Ho, [b] Ee Jin Teo [‡,b] and Andrew A. Bettiol[†,a]

Nanodiamonds (NDs) with nitrogen-vacancy (NV) centers have shown significant potential for nano- and micro-scale local temperature sensing and imaging. However, the challenge lies in achieving non-invasive measurement, due to a high thermal conductivity of diamond that can cause strong thermal spreading and heat dissipation. A solution is to prepare separated NDs for thermal sensing. Here we introduce a method for uniform coating of separated NDs by a rapid thin polymer-assisted electrostatic self-assembly process. This method can be applied to a large scale with a low cost under ambient conditions. Testing with negatively charged carboxylated 100 nm NDs, we demonstrate ND coatings with a controlled area density (up to 1.74×10^9 cm^{-2}) and a low optical transmission loss of 1.21 %. Despite size variation of the NDs, the separated ND coating exhibits a low measurement error of 1.32 °C in thermal mapping between 27 and 80 °C. Furthermore, by steady-state thermal simulations, we show a >7× lower thermal spreading of the separated ND coating compared to a 100 nm thick ND film. This work offers a simple method for large-scale coating of separated NDs, paving a path for achieving non-invasive and accurate ND-based thermal sensing.

Introduction

Nanodiamonds (NDs) containing nitrogen-vacancy (NV) centers have emerged as versatile nanoscale temperature sensors due to their biocompatibility, thermal stability (up to 900 °C[1]), and temperature-sensitive optical and electron spin properties (such as zero-phonon line (ZPL)[2,3], zero-field splitting (ZFS)[4–6], and fluorescence lifetime[7]). These properties enable a broad range of temperature-sensing applications using NDs, including intracellular thermometry[8–13], chemical reaction monitoring[14], scanning probe microscopy[15], and surface thermal imaging[4–6]. However, different application scenarios demand different methods for nanodiamond deployment and signal readout. For instance, intracellular thermometry often requires the use of individual NDs in solution, without any substrate or coating, while NDs for thermal imaging are deposited as a thin film on the surface of the sample. In this work, we target at the application of surface thermal imaging on solid substrates, such as microelectronic surfaces (for locating hot-spots[4,5], etc) or material interface[14]. In such cases, NDs are deposited as a thin film on the surface of the sample, and their spatial distribution directly influences measurement accuracy.

Due to the high thermal conductivity of diamond, achieving non-invasive and accurate thermal imaging presents a significant challenge. If the ND film contains clusters or interconnected NDs, it can lead to lateral thermal spreading across the coating. This lateral spreading acts as a heat sink, smoothing out local temperature gradients and thereby distorting the true spatial distribution of heat. As a result, the temperature measured by an ND may not accurately reflect the temperature at its specific location, especially when NDs contact with each other. For example, on a quartz substrate, 100 nm thick diamond can result in a few micrometers lateral spreading and a more than sixfold reduction of local temperature variation compared to the substrate without diamond[16]. The commonly used spin coating method for ND deposition suffers from low material utilization and poor macroscopic uniformity. Non-uniform coatings can lead to regions with excessive clustering (increasing thermal crosstalk) and others with no coverage (missing data points), both of which degrade the spatial resolution and reliability of thermal imaging. To mitigate thermal spreading, researchers have explored embedding NDs into[3] or attaching them to[5] polymers. However, the measurement accuracy could be influenced by thermal properties of the polymers. The most effective approach is to coat spatially separated NDs in a uniform, well-controlled manner—ensuring each ND acts as an independent, localized sensor with minimal thermal interaction with neighboring NDs. This configuration minimizes thermal cross-talk and preserves spatial fidelity in thermal imaging.

[a] Centre for Ion Beam Applications, Department of Physics, National University of Singapore, 2 Science Drive 3, 117551, Singapore.
[b] Institute of Materials Research and Engineering, 2 Fusionopolis Way, 138634, Singapore.

Corresponding author:
† a.bettiol@nus.edu.sg
‡ teoej@imre.a-star.edu.sg

Supplementary Information available: [AFM image of the P4VP layer, ND coatings using a high P4VP concentration, detailed description of the ODMR system for thermal sensing, ODMR mapping of the ND coating, system errors for the ODMR measurement, fabrication process of Au NPs, and Python code for ND counting.]. See DOI: 10.1039/x0xx00000x

DOI: 10.1039/D5NR02012C

ND coating has been extensively researched in diamond growth industry, typically called diamond seeding, a process prior to the growth of diamond. Among the various techniques that exist for ND coating, including mechanical abrasion[17], electrophoretic deposition[18], Langmuir-Blodgett deposition[19], and electrostatic self-assembly[20–22], electrostatic self-assembly enables fast, uniform, thin film coating of NDs. In this method, NDs are functionalized with ligands of a certain charge while the substrate to be coated has an oppositely charged surface. Thus, by electrostatic force, the NDs can self-assemble on the substrate. However, directly applying the seeding technique to thermal sensing applications faces challenges, because the NDs typically used for seeding are only several nanometers in size with a hydrogen-terminated surface, whereas those intended for thermal sensing range from 50 to 300 nm with oxygen- or nitrogen-terminated surfaces[23]. Changing surface termination from oxygen to hydrogen can convert NV centers from negatively charged state (NV^-) to the neutral state (NV^0)[24], lowering the sensitivity for thermal sensing. Although hydrogenated NDs can be oxidized via oxygen plasma or air annealing to restore the NV^- charge state, but the additional oxidation step can complicate process integration, especially on temperature-sensitive or polymer-coated microelectronic substrates. To coat separated oxygen-terminated NDs for sensing, one solution, reported by Shulevitz et al.[25] and Jiang et al.[26], is by exploiting template-assisted electrostatic self-assembly methods. They use electron beam lithography to fabricate nanostructures as templates for depositing and patterning of separated oxygen-terminated NDs. A recent report by Blankenship et al.[27] shows direct laser writing of ND bubble structures for thermal imaging. Although these methods show state-of-art manipulation of individual NDs at nanoscale, they face challenges such as long processing time, limited-scalability.

A scalable approach to coat oxygen-terminated NDs is electrostatic self-assembly using a thin layer of cationic polymer. This method has been widely used to achieve uniform, high-density coatings of colloidal particles such as polystyrene spheres for lithographic applications[28–30], and has also been extended to NDs. For example, Girard et al.[31] demonstrated the self-assembly of 15–50 nm oxidized NDs on poly(diallyldimethylammonium chloride) (PDDAC), achieving uniform coatings for seeding in diamond film growth. However, their work did not address thermal sensing, and the impact of ND distribution on thermal measurement accuracy was not investigated. Moreover, PDDAC is highly hydrophilic and hygroscopic, which limits its suitability for integration with standard microelectronic platforms and long-term NV^- stability. In this work, we focus on achieving spatially separated NDs to minimize thermal spreading and improve local temperature sensing accuracy. Using a ~5 nm thin layer of poly(4-vinylpyridine) (P4VP), we demonstrate ambient-condition coating of separated NDs with tunable area density. We further evaluate the thermal spreading characteristics via numerical simulation and assess the temperature measurement error through electron spin resonance of NV^- centers. This work provides an alternative method for coating separated NDs for achieving accurate, non-invasive measurements in ND-based thermal sensing applications.

Electrostatic self-assembly of separated NDs

To demonstrate the ND coating, we used commercially available NDs with an average size about 100 nm and a nitrogen-vacancy (NV) concentration of 3 ppm, suspended in deionized (DI) water (NDNV100nmHi, Adamas Nanotechnologies). The size distribution of the NDs is given in Fig S1 in the supporting info. The NDs are oxygen-terminated in the form of carboxylic acids (−C(=O)−OH). Because of deprotonation of carboxylic acids, negatively charged carboxylate ions (−COO−) are formed on the ND surface when they are suspended in DI water. Zeta potential of the ND suspension is -41.2 ± 9.9 mV (measured by Zetasizer Nano, Malvern Panalytical), indicating a strongly negative surface charge and good colloidal stability. This high negative potential suggests effective surface functionalization with carboxylic acids. A higher (absolute) zeta potential can promote the deposition of well-separated NDs because it indicates a stronger attraction to substrate but more repulsion between NDs. The moderate standard deviation indicates some heterogeneity in surface charge distribution, possibly due to variation in ND size or incomplete oxidation. The overall charge is sufficient to enable effective electrostatic self-assembly onto positively charged substrates.

To create positive charge on a sample surface, polymer poly(4-vinylpyridine) (P4VP) (Sigma-Aldrich, Merck Pte. Ltd.) was used. P4VP is a low-cost, versatile polymer that has been widely used in composites, such as block co-polymers, for electrostatic self-assembly of nanoparticles[32,33]. P4VP becomes positively charged in DI water due to its low isoelectric point of 5.1[34]. By coating a P4VP layer on a sample surface, the carboxylated NDs can self-assemble on the sample by the electrostatic force between the carboxylic acids and the P4VP.

Before coating, we first dissolved the P4VP in ethanol to a low concentration of a weight percentage ranging from 1×10^{-4} to 2×10^{-2} %wt. The P4VP layer thickness is measured by AFM on a Si substrate to be 5 nm for the highest concentration of 2×10^{-2} %wt at a spin speed of 3000 rpm for 30 s (see Fig S2 in supporting information). Forming a thin P4VP layer is critical to achieve self-assembly of separated NDs, as illustrated by a simplified electrostatic model in Figure 1(a). Assuming an infinite surface coated with a P4VP layer in the ND suspension, the suspended NDs initially deposit on the surface by the electrostatic force of attraction. The deposited NDs affect the subsequent deposition process because of their repulsion force on the suspended NDs. Since the P4VP layer is so thin that the attractive force on the suspended NDs is relatively weak, repulsion force from the deposited NDs dominates on the suspended NDs when they approach the deposited NDs. This prevents them from contacting with the deposited NDs when they are deposited, thus forming separated NDs on the sample surface. Figure 1(b) shows the coating process. After spin coating the P4VP on the sample, the sample is immersed in the ND suspension for 60 s. Next, the substrate is rinsed in DI water

and dried by blowing air or nitrogen gas over the surface. To remove the P4VP residue, an optional step of plasma cleaning can be applied to the sample surface. In this study, we applied 5 min, high power cleaning with air gas using a basic plasma cleaner (PDC-32G from Harrick Plasma).

Results and discussion

Uniformity and optical transmission of the separated ND coating

Figure 1(c) shows a top-view SEM image of the separated ND coating on a Si substrate. The NDs were prepared by spin coating the Si substrate with 0.02 %wt P4VP and subsequently immersing it in a ND suspension of a concentration of 1 mg/mL for 60 s. From cross-sectional SEM (Figure 1d), the thickness of the ND layer is about 100 nm, which matches with the average size of the NDs, indicating that single NDs are dispersed on the surface. Area density of the NDs is about 1.68×10^9 cm^{-2}, which is counted by skimage package with a ND size threshold of 50 nm (Python code is in the supporting information). The area density corresponds to an average separation distance of ~250 nm, enabling a sufficient spatial resolution since it is beyond the optical diffraction-limited (~400 nm[35]) in NV-based wide field imaging. To evaluate the stability of the ND coating in wet environments, we immersed the ND-coated Si substrate in water and subjected it to ultrasonic cleaning. The coating exhibited a 7% reduction in ND surface density after 90 s of sonication, and a 28% reduction after 270 s, as estimated from the normalized light intensity in dark-field optical images. These results show that the ND coating can withstand short-duration ultrasonic cleaning in aqueous environments (see Fig S3 in supporting info). Although oxygen plasma cleaning removes exposed P4VP residues through an isotropic chemical etching process, the sonication test suggests that the P4VP directly beneath the NDs may be partially shielded by the NDs, therefore, contributes to the ND adhesion.

For thermal sensing with NV centers, a uniform NV emission intensity from the ND coating is crucial to avoid over- or under-exposure of the photodetectors on the sensing area. To obtain the required uniformity, in Figure 1(e), we imaged the NV emission of the ND coating by a confocal microscope (20× obj., N.A. = 0.8, Zeiss LSM780). The uniformity is quantified by relative standard deviation (RSD) which is defined as the ratio of standard deviation (σ) to mean value (μ) in percentage. From the intensity histogram (Figure 1f), we obtained an RSD of 56% for a scan area of 250 × 250 μm^2. The non-uniformity mainly comes the ND size variation of the ND suspension, because ND clustering is insignificant from SEM images (account for only 3%, see Fig S4 in supporting info). The deviation is acceptable for thermal imaging applications. For example, if a photodetector has

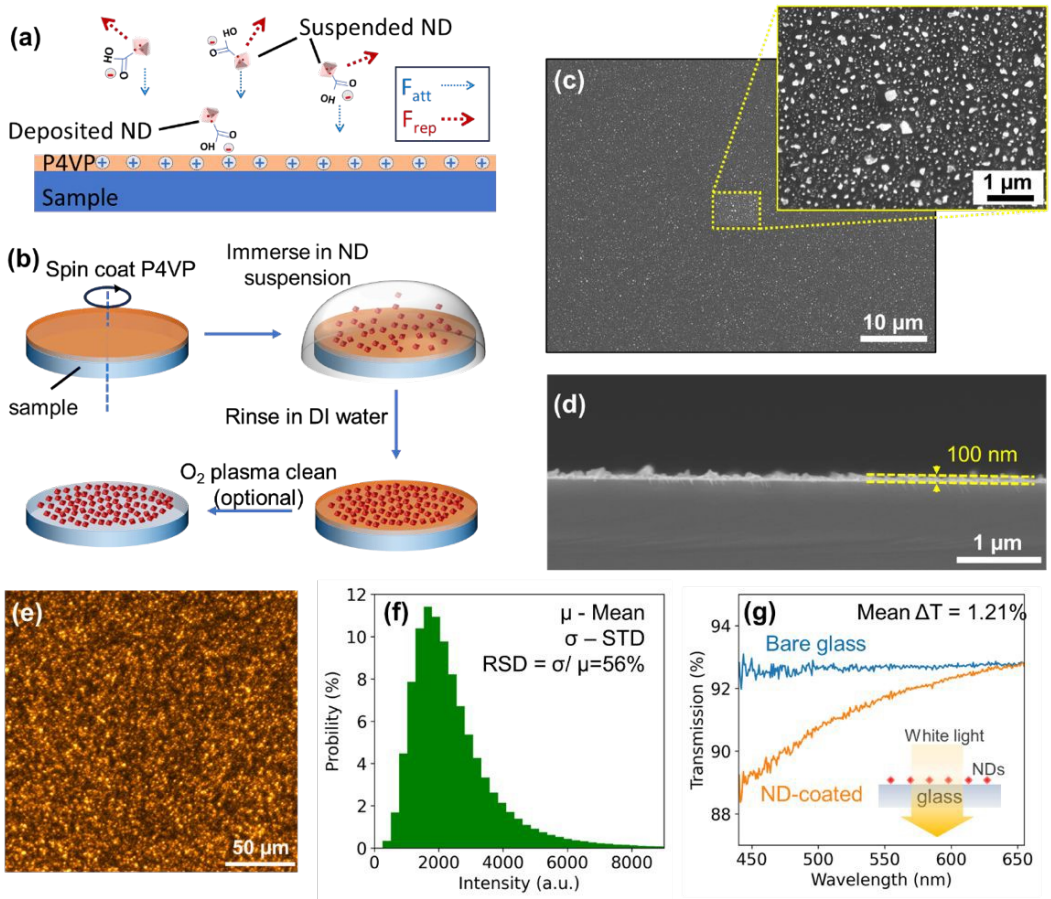

Figure 1. (a) A P4VP-coated sample in a carboxylated ND suspension. The blue arrow and the red arrow represent the attraction force and the repulsion force on the suspended NDs, respectively. (b) Schematic diagram of the coating process. (c) Top and (d) cross-sectional SEM images of the ND coating on a silicon substrate. (e) Confocal image of NV- centers in the ND coating, excited by a 561 nm laser and collected in a wavelength range of 618 to 758 nm. (f) PL intensity distribution of the NV- centers in the confocal image. A relative standard deviation (RSD) is used to quantify uniformity. (g) Optical transmission spectra of bare and ND-coated glass coverslips.

View Article Online
DOI: 10.1039/D5NR02012C

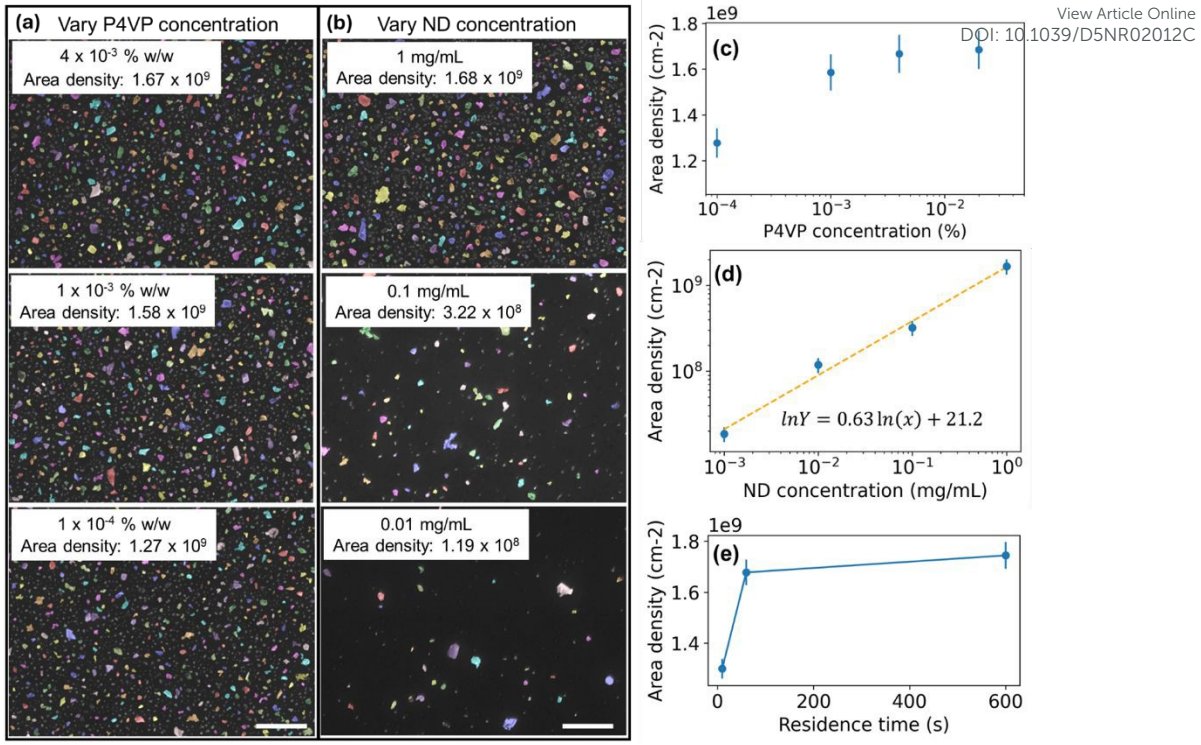

Figure 2. (a) SEM images of ND coatings using different P4VP concentrations at a fixed ND suspension concentration of 1 mg/mL, and a residence time of 60 s. (b) ND coating using different ND suspension concentrations at a fixed P4VP concentration of 0.02 %wt., and a residence time of 60 s. (c) Plot of ND area density as a function of P4VP concentrations. (d) Plot of ND area density as a function of ND concentrations in the suspension. (e) ND area density for different residence times at a fixed P4VP concentration of 0.02% and a ND suspension concentration of 1mg/ml. All the ND area densities are for NDs of a size >50nm. The scale bar in the SEM images represents 1 μm.

a detection limit of 0.1μ to 2μ, where μ is the mean intensity of the NV emission, an RSD of 56% enables the emission from 95.5% of the ND coating area to be within the detection limit.

Optical transmission of the ND coating was measured by coating the NDs on a glass coverslip. Figure 1(g) compares the transmission spectra of the glass with and without the ND coating in a visible spectral range of 450 to 650 nm. Because of Rayleigh scattering of the NDs, the transmission of the ND-coated glass is wavelength-dependent. The loss has a maximum of 4% at 450 nm and decreases as the wavelength increases. On average, the ND coating has a low transmission loss of 1.21% for the visible range.

Area density of the separated NDs.

Density of the NDs is an important factor to thermal sensing because it influences thermal isolation between NDs, as well as thermal emissivity that relates to the surface area of the ND coating. We show that the ND area density can be adjusted by the concentration of the P4VP solution and the ND suspension in the coating process. Figure 2(a) and Figure 2(b) show SEM images of the separated NDs coated by using different concentrations of the P4VP solution and the ND suspension. A fixed residence time of 60 s was used. The ND area density was measured by counting the NDs in the SEM images. Note that NDs with a size of less than 50 nm are excluded from the counting because of their much smaller size than the average and a low NV emission for thermal sensing.

Figure 2(c) plots the ND area density as a function of the P4VP concentrations for a fixed ND concentration of 1 mg/ml. The result shows that the ND area density increases as the P4VP concentration increases from 1×10^{-4} %wt to 2×10^{-2} %wt. This can be explained by a stronger electrostatic attraction force on the NDs that increases the ND deposition rate, because a higher P4VP concentration for spin-coating results in a thicker P4VP layer on the sample surface. As the P4VP concentration further increases beyond 2×10^{-2} %wt, the P4VP surface becomes uneven with a high surface roughness (R_a = 14.6 nm) and causes clustering of NDs (Fig S5 in supporting info).

Figure 2(d) shows a log-log plot of the ND area density as a function of the ND suspension concentration. Compared to the effect of the P4VP concentration on the ND area density, the ND suspension concentration shows a stronger influence on the ND area density, changing it from 1.85×10^7 to 1.68×10^9 cm^{-2} (nearly 2 orders of magnitude) as the ND suspension concentration increases from 1×10^{-3} to 1 mg/ml. They are linearly correlated at logscale with a gradient of 0.63, making control of the ND area density possible by changing the concentration of the ND suspension. The gradient is less than 1, which also implies saturation of the ND density as concentration of ND suspension further increases. The saturation occurs when

View Article Online
DOI: 10.1039/D5NR02012C

the NDs reach a maximum area density that prevents deposition of the NDs in the suspension.

Here we obtained the maximum area density by extending the residence time. Figure 2(e) plots the ND densities for different residence times using the same ND (1 mg/mL) and P4VP (2 × 10^{-2} %wt) concentration. The ND area density begins to saturate at a residence time of 60 s, increasing gradually to approximately 1.74 ± 0.05 × 10^{9} cm^{-2} as the residence time extends to 600 s. The fast saturation time of 60 s indicates a high deposition efficiency, which can be attributed to the large negative zeta potential of the NDs (-41.2 ± 9.9 mV). Zeta potential reflects the surface charge of the particles and governs their interaction with both the substrate and each other. A more negative zeta potential enhances the electrostatic attraction between the NDs and the positively charged P4VP layer, thereby promoting rapid and efficient deposition. At the same time, a high absolute zeta potential also increases interparticle repulsion in the suspension, which limits aggregation and promotes better dispersion. As a result, the maximum area density is influenced by the balance between these two effects: strong attraction to the substrate and mutual repulsion among particles, which ultimately determines the spatial separation between deposited NDs.

Thermal spreading of the ND coating

To evaluate the performance of the ND coating for non-invasive thermal sensing, we numerically studied the thermal spreading of the ND coating using Heat Transfer module in COMSOL Multiphysics. We compared the thermal spreading of 3 configurations: bare glass substrate, glass substrate with the separated ND coating, and glass with a 100-nm thick continuous ND film (thermal conductivity k_{film} = 40 W/(m·K)[36]). Figure 3(a) shows the simulation model of the glass substrate with the separated NDs. The ND coating is simulated as an array of NDs in which each ND is represented by a nanodisk of both a thickness and a diameter of 100 nm. The density of the NDs is determined by the period of the array, annotated as P.

Figure 3(b) shows the temperature distribution of the 3 configurations with localized heating. Only one-quarter of the simulation area is shown because of symmetrical boundary conditions at the XZ and YZ planes. To isolate and accurately evaluate the thermal spreading behavior of the ND coating, we used a point-like source located on the surface of the glass substrate, such as that from a focused laser or microheater tip. In real applications, the heating might be spread out over a larger area, which would reduce temperature differences and

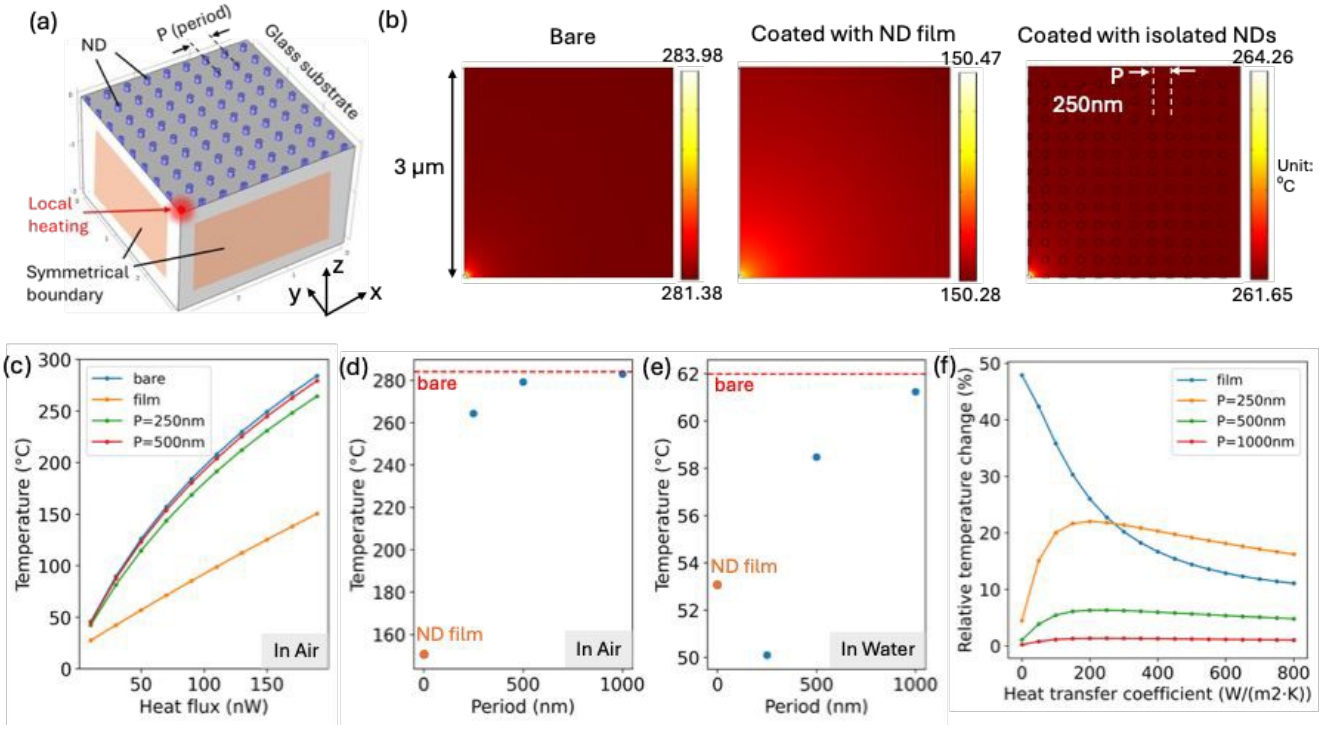

Figure 3. (a) Simulation model for the ND coating on a glass. The separated NDs are represented by a nanodisk array. The local heating area is 50 × 50 nm^2, shown at the top front corner. Symmetrical boundary conditions are applied at the XZ and YZ planes. (b) Simulated temperature distribution for a bare glass, a glass with a 100nm thick nanodiamond (ND) film, and a glass with the separated ND coating. The same input flux of 190 nW was used. P is the period of the ND array. The environment is air. A heat transfer coefficient of 10 W/(m^2·K) is applied to the top surface to include thermal dissipation from air in free convection. (c) A plot of the maximum local temperature at the heating spot as a function of input heat flux. (d) The maximum local temperatures for different periods of the ND arrays in air and (e) in water at the flux input of 190 nW. The dash line is the local temperature of a bare glass. A heat transfer coefficient h = 500 W/(m^2·K) is used to represent the water environment. (f) Plots of relative temperature change ($\Delta T/T_{bare}$) as a function of the heat transfer coefficient applied to the top surface. Thermal conductivity in simulation for the ND array, the ND film, and the glass substrate is k_{ND} = 2200 W/(m·K), k_{film} = 40 W/(m·K), and k_{glass} = 1.38 W/(m·K), respectively.

View Article Online DOI: 10.1039/D5NR02012G

make thermal spreading less noticeable. However, the use of a localized heat source allows for a clearer assessment of how ND spatial distribution impacts local temperature variation. Here we set the heat source to have an input flux of 190 nW and an area of 50 × 50 nm^2. The bare glass, which is used as a reference, is calculated to reach a maximum temperature of 283.97 °C at the heating spot. For the glass coated with a ND film, due to thermal spreading, the temperature drops to 150.39 °C which is 47 % lower than that of the bare glass. This indicates that using a ND film for thermal sensing is invasive to measurement and can substantially underestimate the actual temperature of a sample when the ND film is absent. In contrast, the glass coated with the ND array with a period of 250 nm shows a local temperature of 264.25 °C, only 6.7 % lower than that of a bare glass. The period of 250 nm is chosen because it corresponds to an ND area density of 1.6 × 10^9 cm^{-2}, near to the saturation density of our ND coating. Compared with the ND film coating, the separated ND coating exhibits 7× lower temperature variation, which is consistent with the simulation result reported in the reference[16]. In addition, time-dependent simulations (Fig. S6, Supporting info) show that the ND-array–coated glass exhibits a similar transient response to bare glass, while the ND-film–coated glass displays a faster thermal response due to thermal spreading which enhances heat distribution during rapid thermal events. Therefore, a separated ND coating is also important for an accurate transient temperature measurement.

To study the effect of the ND area density on thermal spreading, we changed the period of the ND array and calculated the local temperature at the heating spot at different input fluxes, shown in Figure 3(c). We found a lower temperature variation for a larger period of the ND array (a lower ND density). When the period increases to 1000 nm (corresponding to an area density of 1 × 10^8 cm^{-2}), the variation between the ND-coated glass and the bare glass becomes negligible (< 0.5 %) (see Figure 3(d)). Since thermal sensing is often performed in wet environments, we extended our simulation to include this condition by applying a heat transfer coefficient of 500 W/(m^2·K) to the top surface, representing convective heat loss to water. Using the same input heat flux, the presence of water significantly reduces the local temperature. On bare glass, the local temperature at the heat source is 61.99 °C (dash line in Figure 3(e)). When the surface is coated with a ND film, the temperature decreases to 53.06 °C, a 14.4 % reduction compared to the bare glass. For the ND arrays with periodicities of 500 nm and 1000 nm, the temperature are 58.47 °C and 61.23 °C, lower by 5.7 % and 1.2 %, respectively, which are close to the bare glass case. However, when the ND array has a small period of 250 nm, the temperature drops shaprly to 50.10 °C, a 19.2% reduction compared to bare glass and even lower than that of the ND film. These results indicate that in wet environments, high-density ND coatings can result in underestimation of the local temperature.

To evaluate the influence of environmental conditions on the thermal sensing behaviour of the ND coating, we calculated the relative temperature variation as a function of the heat transfer coefficients (h), ranging from 0 to 800 W/(m^2·K), shown in Figure 3(f). The relative temperature variation is defined as $\Delta T/T_{bare}$, where T_{bare} is the local temperature on the bare substrate, ΔT is the temperature difference between the ND-coated and bare substrate cases. At low h, ND arrays exhibit significantly smaller temperature variations than the continuous ND film, indicating superior performance for non-invasive sensing under minimal convective losses. However, as h increases, the ND arrays exhibit a rising temperature variation, peaking near h = 200 W/(m^2·K), and then decreases gradually. We attribute this trend to the increased surface area introduced by the ND coating. Particularly, the array with a 250 nm period, which has approximately 50% higher surface area than the ND film, shows greater thermal dissipation at a high h. These results suggest that in highly convective environment, the increased surface area of dense ND coatings can enhance heat transfer to the surroundings, lowering the local temperature and resulting in underestimation in thermal measurements. Although the result indicates that a lower ND density is better for non-invasive measurement in both dry and wet environments, we shall note that the ND density determines the spatial resolution in thermal imaging. Therefore, the optimal ND density depends on the requirement of applications, for example, a higher area density would be preferred for imaging while a lower density is more accurate for probing of a local temperature.

Thermal sensing with the ND coating

We demonstrate thermal sensing with the separated ND coating by measuring the electron spin resonance of the NV-centers. NV- centers have unique electron spin properties that exhibit temperature-sensitive zero-field-splitting (ZFS) frequency (the energy gap between spin ±1 states and spin 0 state). We built a lock-in based ODMR system[37] with temperature control to study the performance of the ND coating in temperature sensing, shown in Figure 4(a). A detailed description of the measurement is given in the supporting information (Fig S7).

Before sensing, a calibration process was conducted to obtain the relation between the ZFS frequency and the temperature. Figure 4(b) shows ODMR spectra of the NV-centers at different temperatures from 27.7 ºC to 80.1 ºC. The ZFS frequency can be observed from the peak in the ODMR spectrum, at about 2860-2870 MHz. The occurrence of two peaks in each spectrum is due to lattice strain of the NDs that splits the degenerate spin ±1 states. Note that the electrons in the ±1 states exhibit a lower fluorescence compared to the electrons in the 0 state. The lock-in amplifier measures the absolute difference of the NV emission with and without the microwave (MW), therefore, the resonance is shown as a peak rather than a dip.

To obtain the ZFS frequency, we fitted each ODMR spectrum by 2-Lorentzian function:

$$L(f) = \frac{a \cdot \gamma_1}{\gamma_1^2 + (f - f_1)^2} + \frac{b \cdot \gamma_2}{\gamma_2^2 + (f - f_2)^2} + c$$

View Article Online
DOI: 10.1039/D5NR02012C

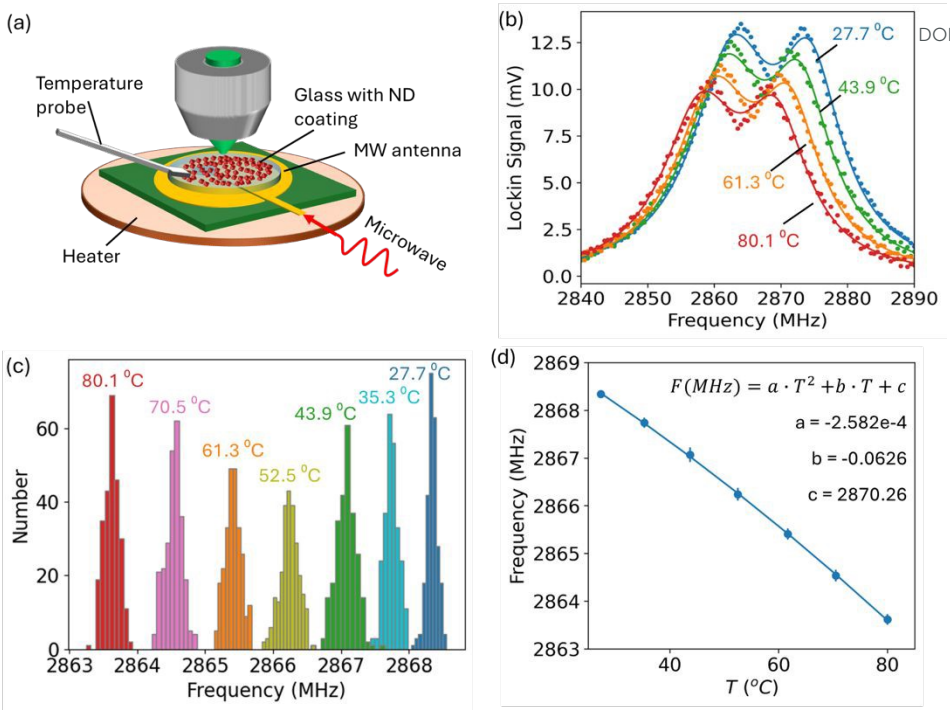

Figure 4. (a) ODMR setup for thermal sensing. (b) ODMR spectra of the NV centers at different temperatures and fitted with 2-Lorentzian function. (c) Histogram of the zero-field-splitting (ZFS) frequencies of NV centers at different temperatures, obtained from 256 spots on the ND coating. (d) Plot of ZFS as a function of temperature and fitted with quadratic polynomial.

where f is the MW frequency, f_1 and f_2 are central frequencies, and a, b, c are constants. The ZFS is determined by the average of the two central frequencies ($\frac{f_1+f_2}{2}$).

As each ND is unique, exhibiting different temperature dependencies, a ND coating often shows a spreading of the ZFS frequency in thermal imaging or mapping. Such spreading limits temperature accuracy and causes measurement error for thermal sensing. Here we measured the temperature dependence of NV- spin resonance from 256 spots in the ND coating (Fig S8 in supporting info). The ZFS frequencies of the spots at different temperatures were plotted in the histogram in Figure 4(c). By measuring the standard deviation (STD) of the ZFS spreading at each temperature, we obtained a measurement error ranging from ±1.0 to ±1.7 °C in 27 to 80 °C with an average value of ±1.32 °C. This error is 3 times lower than those reported measurement errors (about ±3.9 °C) using spin-coated ND films[3,5]. Since NDs of the same size from the same supplier were used in our work and in the reports, the difference due to different inhomogeneity of NDs can be negligible. We found a large difference in terms of system errors. Our system error is about ±0.64 °C (Fig S9 in supporting info), while it is ±2.17 °C in the report[3]. We think one of the reasons that cause the difference in system error could be due to the formation of ND clusters. ND clusters are much brighter than a single ND, which require lowering the sensitivity of a photodetector to avoid over-exposure. This can cause a poor signal-to-noise ratio and a high system error in areas where the NV emission is much lower than the clustered areas. Further reducing measurement error can be achieved by optimizing the ND size distribution, as the NDs used in this study exhibit a relatively broad size range (see Fig. S1 in Supporting Info). Using smaller or more monodisperse NDs could improve the accuracy of area density estimation and reduce variability in thermal response. However, smaller NDs often exhibit weaker NV emission and reduced ODMR contrast, which may compromise thermal sensing sensitivity. These factors present trade-offs in optimizing ND size for thermal sensing applications. The calibration of the ZFS frequency against temperature was carried out by fitting the relation between ZFS and temperature, as plotted in Figure 4(d). A quadratic polynomial function was used to fit the curve, given by: $F\,(MHz) = a \cdot T^2 + b \cdot T + c$, where a = -2.582 × 10^{-4} (MHz·°C^{-2}), b = -0.0626 (MHz·°C^{-1}), c = 2870.26 (MHz). The fitting result is found to be consistent with that reported by Taras et.al.[38] obtained from temperature dependence of 10 NDs.

We show applications of the ND coating as a local thermal sensor to probe the temperature of gold nanoparticles (Au NPs). Au NPs have extraordinary thermo-optical properties, such as strong optical absorption by excitation of localized surface plasmon, making them efficient nanoscale heaters for optical and biomedical applications[39]. But detecting local temperature of Au NPs can be a challenge using a thermal camera, due to a limited spatial resolution, therefore, requiring a nanoscale probe to monitor their temperatures. NDs are one of the promising nanoprobes that can be attached to the Au NPs to build a hybrid optical nanoheater[40]. Here we build a temperature-controllable optical heater by coating the separated NDs on a layer of Au NPs (Figure 5(a)). The Au NPs were fabricated by thermal annealing of a 4 nm thick Au film on a glass substrate at 300 °C for 2 hours in air (Fig S10 in supporting info). A focused 532 nm laser was used for both

View Article Online
DOI: 10.1039/D5NR02012C

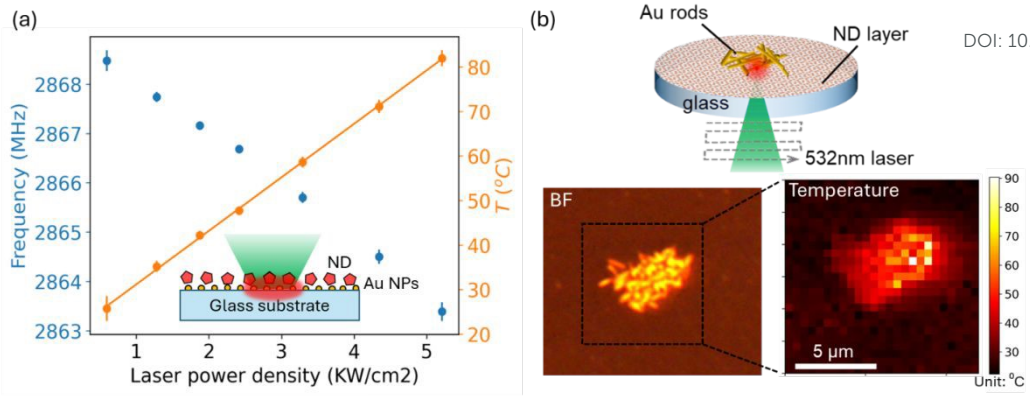

Figure 5. (a) ZFS frequency of NV centers (in blue) and the temperature (in orange) as a function of laser power density. Temperature is calculated by inputting the ZFS to the calibration function and is fitted with a linear equation. Inset: schematic diagram of the optical heater which consist of a ND coating on a layer of gold nanoparticles. (b) Top: schematic diagram of laser heating on the gold nanorods (GNRs) deposited on the ND coating. Bottom: bright field image and thermal mapping of the GNR ensemble.

heating the Au NPs and probing the temperature of the NDs. Figure 5(a) shows the ZFS and temperature of the NDs as a function of the laser power density. As the laser power increases, the ZFS frequency of the NV centers redshifts, indicating temperature increase with the laser power. Since the absorbed energy is proportional to the laser power, we observed a linear relationship between the temperature of the NDs and the laser power. We measured the laser power dependences from 25 spots in the ND coating and obtained a temperature accuracy of the optical heater to be about ±1.50 °C (Fig S11 in supporting info). This accuracy is comparable to quantum dots or upconverting nanoparticles-based thermometry[41] and close to single ND-based thermometry (±1.0 °C)[42]. Considering the high biocompatibility and chemical inertness of NDs, such a planar optical heater can be a promising biological or chemical sensing platform for studying thermal response of single cells or for local temperature control of chemical reactions. As another example, Figure 5(b) shows thermal mapping of an ensemble of gold Nanorods (GNRs) using the ND coating. The ensemble consists of GNRs with a diameter of 100 nm and a length of 1 μm, deposited on a ND-coated glass substrate. A focused 532 nm laser with a power of 14 mW was scanned over the GNRs at a scan size of 12 by 12 μm^2 and a step of 0.5 μm. The thermal map, which is read-out from the NDs, shows laser heating of the GNRs as the laser spot scans over the GNR area. This preliminary result indicates potential applications of using the ND coating to investigate hotspots in optical or plasmonic devices.

Conclusions

In conclusion, we have demonstrated a simple, rapid method for coating separated NDs for non-invasive local thermal sensing and imaging. The method relies on the electrostatic self-assembly between a weak positively charged thin polymer and the negatively surface charged NDs in a suspension. Using the 100 nm carboxylated NDs and the P4VP polymer solutions, we show a high uniformity and optical transmission of the ND coating, and control of the ND area density from 1.85×10^7 to 1.68×10^9 cm^{-2} by simply changing the concentration of the ND suspension in the coating process. By thermal simulation, we show a 7× lower local temperature variation of the separated ND coating compared to a ND film in probing local temperatures. Confocal and SEM imaging have shown a uniform density distribution of the ND coating, free of ND clusters, leading to a low measurement error in temperature mapping. Our result shows that the ND coating can be promising for localized temperature monitoring, for example, by combining the NDs with Au NPs to build a localized heater and sensor, or using as a sensing platform for investigating thermal properties of nanomaterials that are hardly measured by thermal cameras. We envision that the ND coating can also be applied to wide-field thermal imaging of micro-electronics or photonics to investigate hot spots or device reliability. Additionally, attributed to the excellent biocompatibility and durability of NDs, the ND coating could also give new solutions to applications such as anti-fouling[43] or anti-dusting. Beyond optimizing the coating process, further enhancements in thermal sensing performance may be achieved by tailoring intrinsic nanodiamond properties. For example, increasing NV concentration through electron irradiation and annealing[44], modifying surface termination to stabilize the NV^- charge state[45], or using isotopically pure diamond can improve spin coherence and temperature sensitivity[46]. These strategies are complementary to our method and represent promising future directions for advancing ND-based thermal sensing.

Author contributions

C. Yang carried out the simulation and optical measurement. C. Yang, V. Suresh, E. J. Teo and A. A. Bettiol conceived of the idea. A. S. Rotelli prepared the Au nanoparticles. H. Sun carried out preparation of P4VP solutions. V. X. Ho set up the lock-in amplifier for ODMR measurement. The manuscript was written through contributions of all authors. All authors have given approval to the final version of the manuscript.

Conflicts of interest

There are no conflicts to declare.

Data availability

Data for this article has been deposited in the Zenodo repository at https://doi.org/10.5281/zenodo.15403899. The Python code for ND counting is available in the supporting information.

Acknowledgements

We would like to acknowledge the financial support from Ministry of Education (Singapore) Tier 2 Grant MOE-T2EP50221-0009, A*STAR (Singapore) Grant A-8001285-03-00, and the funding from MTI-IRG under Grant number M24N7c0094 on "Wide field-of-view and high gain fluorescent-lens system for simultaneous optical tracking and communications" and A*STAR (Singapore) under CRF-ATR on "Omnidirectional Fluorescent Concentrator for Robust, Sustainable Optical Wireless Communications".

References

1 H. Ozawa, H. Ishiwata, M. Hatano and T. Iwasaki, *physica status solidi (a)*, 2018, **215**, 1800342.
2 M. Fukami, C. G. Yale, P. Andrich, X. Liu, F. J. Heremans, P. F. Nealey and D. D. Awschalom, *Physical Review Applied*, 2019, **12**, 014042.
3 Y. Y. Hui, O. Y. Chen, T. Azuma, B. M. Chang, F. J. Hsieh and H. C. Chang, *Journal of Physical Chemistry C*, 2019, **123**, 15366–15374.
4 C. Foy, L. Zhang, M. E. Trusheim, K. R. Bagnall, M. Walsh, E. N. Wang and D. R. Englund, *ACS Appl. Mater. Interfaces*, 2020, **12**, 26525–26533.
5 P. Andrich, J. Li, X. Liu, F. J. Heremans, P. F. Nealey and D. D. Awschalom, *Nano Letters*, 2018, **18**, 4684–4690.
6 K. Ogawa, M. Tsukamoto, K. Sasaki and K. Kobayashi, *Journal of the Physical Society of Japan*, 2023, **92**, 1.
7 D. K. Bommidi and A. D. Pickel, *Applied Physics Letters*, 2021, **119**, 25.
8 S. Sotoma, C. Zhong, J. C. Y. Kah, H. Yamashita, T. Plakhotnik, Y. Harada and M. Suzuki, *Sci. Adv.*, 2021, **7**, eabd7888.
9 S. Sotoma, C. P. Epperla and H. Chang, *ChemNanoMat*, 2018, **4**, 15–27.
10 A. M. Romshin, V. Zeeb, A. K. Martyanov, O. S. Kudryavtsev, D. G. Pasternak, V. S. Sedov, V. G. Ralchenko, A. G. Sinogeykin and I. I. Vlasov, *Scientific Reports*, 2021, **11**, 1.
11 A. M. Romshin, V. Zeeb, E. Glushkov, A. Radenovic, A. G. Sinogeikin and I. I. Vlasov, *Scientific Reports*, 2023, **13**, 1.
12 Y. Wu and T. Weil, *Advanced Science*, 2022, **9**, 19.
13 G. Kucsko, P. C. Maurer, N. Y. Yao, M. Kubo, H. J. Noh, P. K. Lo, H. Park and M. D. Lukin, *Nature*, 2013, **500**, 54–58.
14 R. Dou, Z. Li, G. Zhu, C. Lin and B. Wang, *Diamond and Related Materials*, 2023, **140**, A.
15 A. Laraoui, H. Aycock-Rizzo, Y. Gao, X. Lu, E. Riedo and C. A. Meriles, *Nature Communications*, 2015, **6**, 8954.
16 R. Tanos, W. Akhtar, S. Monneret, F. Favaro de Oliveira, G. Seniutinas, M. Munsch, P. Maletinsky, L. le Gratiet, I. Sagnes, A. Dréau, C. Gergely, V. Jacques, G. Baffou and I. Robert-Philip, *AIP Advances*, 2020, **10**, 025027.
17 S. Mandal, *RSC Advances*, 2021, **11**, 10159–10182.
18 A. M. Affoune, B. L. V. Prasad, H. Sato and T. Enoki, *Langmuir*, 2001, **17**, 547–551.
19 V. Pichot, K. Bonnot, N. Piazzon, M. Schaefer, M. Comet and D. Spitzer, *Diamond and Related Materials*, 2010, **19**, 479–483.
20 T. Yoshikawa, N. Tokuda, Y. Makino, A. Tsurui, R. Ieki, R. Kojima, M. Liu, T. Mahiko and M. Nishikawa, *Carbon Trends*, 2022, **9**, 100202.
21 J. Hees, A. Kriele and O. A. Williams, *Chemical Physics Letters*, 2011, **509**, 12–15.
22 T. Yoshikawa, M. Reusch, V. Zuerbig, V. Cimalla, K.-H. Lee, M. Kurzyp, J.-C. Arnault, C. Nebel, O. Ambacher and V. Lebedev, *Nanomaterials*, 2016, **6**, 217.
23 M. Fujiwara and Y. Shikano, *Nanotechnology*, 2021, **32**, 482002.
24 M. V. Hauf, B. Grotz, B. Naydenov, M. Dankerl, S. Pezzagna, J. Meijer, F. Jelezko, J. Wrachtrup, M. Stutzmann, F. Reinhard and J. A. Garrido, *Physical Review B*, 2011, **83**, 081304.
25 H. J. Shulevitz, T.-Y. Huang, J. Xu, S. J. Neuhaus, R. N. Patel, Y. C. Choi, L. C. Bassett and C. R. Kagan, *ACS Nano*, 2022, **16**, 1847–1856.
26 M. Jiang, J. A. Kurvits, Y. Lu, A. V. Nurmikko and R. Zia, *Nano Letters*, 2015, **15**, 5010–5016.
27 B. W. Blankenship, J. Li, Z. Jones, M. Parashar, N. Zhao, H. Singh, R. Li, S. Arvin, A. Sarkar, R. Yang, T. Meier, Y. Rho, A. Ajoy and C. P. Grigoropoulos, *Nano Letters*, 2024, **24**, 9711–9719.
28 T. Serizawa, S. Kamimura and M. Akashi, *Colloids and Surfaces A*, 2000, **164**, 2, 237-245.
29 H. Y. Koo, D. K. Yi, S. J. Yoo and D. Y. Kim, *Advanced Materials*, 2004, **16**, 274–277.
30 P. Hanarp, D. S. Sutherland, J. Gold and B. Kasemo, *Colloids and Surfaces A: Physicochemical and Engineering Aspects*, 2003, **214**, 23–36.
31 H. A. Girard, S. Perruchas, C. Gesset, M. Chaigneau, L. Vieille, J.-C. Arnault, P. Bergonzo, J.-P. Boilot and T. Gacoin, *ACS Appl. Mater. Interfaces*, 2009, **1**, 2738–2746.
32 V. Suresh and F. L. Yap, *RSC Adv.*, 2015, **5**, 61671–61677.
33 Y. Zhao, K. Thorkelsson, A. J. Mastroianni, T. Schilling, J. M. Luther, B. J. Rancatore, K. Matsunaga, H. Jinnai, Y. Wu, D. Poulsen, J. M. J. Fréchet, A. Paul Alivisatos and T. Xu, *Nature Mater*, 2009, **8**, 979–985.
34 G. Douyère, L. Leclercq and V. Nardello-Rataj, *Colloids and Surfaces A: Physicochemical and Engineering Aspects*, 2021, **631**, 127705.
35 S. C. Scholten, A. J. Healey, I. O. Robertson, G. J. Abrahams, D. A. Broadway and J.-P. Tetienne, *Journal of Applied Physics*, 2021, **130**, 150902.
36 J. Anaya, S. Rossi, M. Alomari, E. Kohn, L. Tóth, B. Pécz, K. D. Hobart, T. J. Anderson, T. I. Feygelson, B. B. Pate and M. Kuball, *Acta Materialia*, 2016, **103**, 141–152.
37 V. K. Sewani, H. H. Vallabhapurapu, Y. Yang, H. R. Firgau, C. Adambukulam, B. C. Johnson, J. J. Pla and A. Laucht, *American Journal of Physics*, 2020, **88**, 1156–1169.
38 T. Plakhotnik, M. W. Doherty, J. H. Cole, R. Chapman and N. B. Manson, *Nano Letters*, 2014, **14**, 4989–4996.
39 A. Guglielmelli, F. Pierini, N. Tabiryan, C. Umeton, T. J. Bunning and L. D. Sio, *Advanced Photonics Research*, 2021, **2**, 200198.
40 P.-C. Tsai, O. Y. Chen, Y.-K. Tzeng, Y. Y. Hui, J. Y. Guo, C.-C. Wu, M.-S. Chang and H.-C. Chang, *EPJ Quantum Technol.*, 2015, **2**, 19.
41 L. Jauffred, A. Samadi, H. Klingberg, P. M. Bendix and L. B. Oddershede, *Chemical Reviews*, 2019, **119**, 8087–8130.

View Article Online
DOI: 10.1039/D5NR02012C

42 Y.-K. Tzeng, P.-C. Tsai, H.-Y. Liu, O. Y. Chen, H. Hsu, F.-G. Yee, M.-S. Chang and H.-C. Chang, *Nano Lett.*, 2015, **15**, 3945–3952.
43 S. Zhou, Z. Zhou, Y. Liu, W. Liu, B. Da, Y. Zhao, S. Handschuh-Wang and T. Wang, *Materials Chemistry and Physics*, 2024, **317**, 129172.
44 M. Capelli, A. H. Heffernan, T. Ohshima, H. Abe, J. Jeske, A. Hope, A. D. Greentree, P. Reineck and B. C. Gibson, *Carbon*, 2019, **143**, 714–719.
45 J. N. Neethirajan, T. Hache, D. Paone, D. Pinto, A. Denisenko, R. Stöhr, P. Udvarhelyi, A. Pershin, A. Gali, J. Wrachtrup, K. Kern and A. Singha, *Nano Lett.*, 2023, **23**, 2563–2569.
46 J. E. March, B. D. Wood, C. J. Stephen, L. D. Fervenza, B. G. Breeze, S. Mandal, A. M. Edmonds, D. J. Twitchen, M. L. Markham, O. A. Williams and G. W. Morley, *Phys. Rev. Applied*, 2023, **20**, 4.

View Article Online
DOI: 10.1039/D5NR02012C

Data Availability Statement (DAS)

Data for this article has been deposited in the Zenodo repository and is publicly available at: https://doi.org/10.5281/zenodo.15403899. The Python code for ND counting is available in the supporting information.